East European Journal of Physics. 2. 622-632 (2026)
DOI:10.26565/2312-4334-2026-2-69 ISSN 2312-4334

EPITAXIAL STABILIZATION AND RADIATION-STIMULATED SEGREGATION IN CA-PVD AlN/CrN MULTILAYER COATINGS UNDER ION BOMBARDMENT

O.V. Maksakova*, V.M. Beresnev, S.V. Lytovchenko, R.S. Galushkov
V.N. Karazin Kharkiv National University, 4, Svoboby Sq., 61000 Kharkiv, Ukraine
**Corresponding Author e-mail: o.maksakova@karazin.ua*
Received February 2, 2026; revised April 10, 2026; accepted April 20, 2026

This paper investigates the regularities governing the formation of the atomic-crystalline architecture, surface topography, and chemical composition of AlN/CrN multilayer coatings deposited via cathodic arc physical vapor deposition onto AISI 321 austenitic stainless-steel substrates. The synergistic effect of the negative substrate bias voltage (–50, –100, and –200 V) and the deposition duration of individual AlN layers (10, 40, and 60 s) on the kinetics of phase competition and the evolution of radiation-stimulated nanostructures was analyzed. Using X-ray diffraction and scanning electron microscopy, combined with energy-dispersive X-ray spectroscopy, it was established that at low deposition energies (–50 V, 10 s), the epitaxial template effect of the c-CrN matrix dominates, thereby stabilizing the metastable cubic c-AlN phase. Increasing both the layer thickness and the substrate bias to –100 V leads to the breakdown of pseudomorphic growth and transitions the system into a possible nanocrystalline or quasi-amorphous state. At high bias potential of -200 V, complete thermal relaxation occurs, accompanied by a textured phase transition of AlN into its stable hexagonal wurtzite modification (h-AlN). A counterintuitive decrease in the aluminum concentration (from 46.88 to 33.72 at. %) despite the prolonged growth time was observed. This phenomenon is driven by the selective re-sputtering of lighter Al atoms under the influence of a high-energy ion flux. Furthermore, radiation-stimulated interdiffusion of iron from the substrate into the coating, along with an ion-cleaning effect that removes interstitial carbon impurities from the matrix, was recorded. The insights obtained expand current understanding of non-equilibrium solid-state thermodynamics and open new possibilities for the precision tailoring of nanostructured protective coatings by optimizing ion-plasma parameters.
Keywords: *PVD; Nitrides; Multilayer coatings; AlN; CrN; Microstructure; Chemical composition; Phase state*
PACS: 68.55.Jk, 68.65.Ac

1. INTRODUCTION

In the context of the intensive development of modern condensed matter physics, ion-plasma technologies, and materials science of extreme states, a fundamental understanding of structure-formation processes in thin-film heterophase systems is of paramount importance. The investigation of the atomic-crystalline architecture of films synthesized under non-equilibrium conditions of high-energy ionic bombardment allows for the revelation of profound physical aspects of phase stability, the regularities governing the formation of metastable states, and the specific features of interfacial mass transfer. Unlike classical applied approaches that focus exclusively on recording macroscopic performance characteristics, the analysis of substructural variations reveals regularities in atomic diffusion, lattice relaxation, and energy balance at nanolayer interfaces [1, 2]. Structural investigations using X-ray diffraction (XRD), scanning electron microscopy (SEM), and energy-dispersive X-ray spectroscopy (EDS) are key tools for verifying theoretical models of non-equilibrium solid-state thermodynamics [3].

Among the diverse binary and ternary nitride systems, the combination of aluminum nitride (AlN) and chromium nitride (CrN) is of particular fundamental interest. The physical appeal of investigating this specific pair lies in the unique combination of their individual structural constants, thermodynamic parameters, and coordination geometries [4]. While chromium nitride forms a stable cubic lattice of the NaCl-type (space group $Fm\bar{3}m$, B1 structure) with octahedral atomic coordination at room temperature and atmospheric pressure, aluminum nitride under identical conditions crystallizes into a stable hexagonal wurtzite modification (space group $P6_3mc$, B4 structure) featuring tetrahedral coordination [5]. Combining two phases with distinct lattice symmetries and different coordination numbers (CN = 6 for CrN and CN = 4 for AlN) within a single thin-film system establishes conditions for severe structural competition and localized lattice instability [6].

The physical structure of these coatings is highly intricate, both in single-layer form (an unmixed ternary alloy, Al-Cr-N) and in multilayer periodic architectures. In single-layer configurations, research primarily focuses on the solubility limit of aluminum in the cubic lattice of CrN, forming a supersaturated substitutional solid solution, c-$Al_xCr_{1-x}N$ [2]. Replacing Cr atoms with Al atoms, which possess a smaller atomic radius, induces severe local lattice distortion, alters interplanar distances, and elevates the internal free energy of the system [6]. Upon reaching a critical Al concentration, a first-order phase transition occurs, accompanied by the collapse of the cubic symmetry and the precipitation of the hexagonal h-AlN phase [5, 9].

Transitioning to a multilayer periodic architecture opens up entirely new physical phenomena, the key among which is the epitaxial (pseudomorphic) stabilization of metastable phases [1, 7]. When the thickness of individual AlN

Cite as: O.V. Maksakova, V.M. Beresnev, S.V. Lytovchenko, R.S. Galushkov, East Eur. J. Phys. 2, 622 (2026), https://doi.org/10.26565/2312-4334-2026-2-69

nanolayers is compressed below a certain critical threshold, the coherent matching at the interfaces with the cubic CrN matrix forces the aluminum atoms to rearrange from a tetrahedral to an octahedral configuration [7]. This effectively results in the artificial stabilization of the high-pressure metastable cubic phase, c-AlN (NaCl-type), under ambient pressure conditions [1, 11]. Investigating the specific conditions under which this epitaxial constraint breaks down – thereby giving rise to diffuse halos and the subsequent relaxation of the system into the hexagonal wurtzite structure – stands as a fundamental problem in solid-state physics [5, 11].

The realization of such complex non-equilibrium states requires the deployment of high-energy techniques for plasma flux generation, among which cathodic arc deposition possesses the highest kinetic and thermodynamic efficiency [1, 3]. The physical essence of the cathodic arc process lies in the evaporation of the cathode material within localized arc spots, ensuring virtually 100% ionization of the working gas-metal flux and generating multiply charged ions (Al^{+}, Al^{2+}, Cr^{+}, Cr^{2+}, Cr^{3+}) [1, 10]. In contrast to conventional magnetron sputtering, where the average particle energy rarely exceeds several electron volts, cathodic arc technology ensures that ions arrive at the substrate with an intrinsic kinetic energy of 20 to 100 eV even before an external bias is applied [1, 8].

The uniqueness introduced by cathodic arc technology in AlN/CrN coatings stems from the ability to exert deep control over the phase composition via radiation-stimulated mass transfer mechanisms [2, 3]. Applying a negative substrate bias voltage accelerates the ion flux, thereby transforming the plasma potential energy into the kinetic energy of collision cascades on the surface of the growing film [8, 10]. This yields a series of unique structural effects. The first of them is a dynamic control over texture and defect formation. High-energy ion assistance drives the directed generation of point defects (vacancies and interstitials), thereby altering interatomic diffusion parameters and forcing the lattice to crystallize along rigorously predefined crystallographic orientations [8]. The second one is the effect of mass-dependent preferential re-sputtering. At extreme substrate biases, high-energy ions begin to selectively eject the lighter Al atoms (m_{Al} = 26.98 amu) compared to the heavier Cr atoms (m_{Cr} = 52.00 amu) from the already formed lattice [5]. This leads to unique stoichiometric shifts that run counter to the classical kinetic laws, which are strictly governed by deposition time [10]. The third effect is the presence of the cathodic droplet phase. A specific microstructural element of the cathodic arc method– – microdroplets ejected from the cathode target – creates a unique heterogeneous surface topography [1, 4]. These droplets act as localized centers of deformation and shadowing, tilting the growth trajectories of columnar grains and uniquely contributing to X-ray diffraction patterns due to verified phase discrepancies between the droplet body and its immediate periphery [1, 2].

The present research represents the precision analysis of the structural-phase and elemental transformations in AlN/CrN multilayer coatings (MLCs) deposited via CA-PVD onto AISI 321 austenitic stainless-steel substrates under the synergistic variation of energetic and temporal parameters. Throughout the experiments, the negative substrate bias voltage was systematically varied across critical points of energetic impact (–50 V, –100 V, and –200 V). Concurrently, the deposition duration of the individual AlN layers was sequentially adjusted to 10, 40, and 60 seconds.

The primary objective of this study is to uncover the fundamental physical causes behind the alterations in XRD diffraction profiles, topographical modifications captured by SEM, and the redistribution of elemental sublattices (including the behavior of impurity carbon atoms and interdiffusional iron originating from the substrate) monitored via EDS. The insights obtained expand current understanding of phase-competition kinetics and ion-stimulated evolution of nanostructures in the highly non-equilibrium thermodynamic environment of a cathodic arc plasma.

2. EXPERIMENTAL DETAILS

2.1. Deposition

The AlN/CrN MLCs were deposited by ion-plasma deposition (CA-PVD) in a reactor-type vacuum chamber (Bulat-6) equipped with two arc evaporators. Technically pure, separate aluminum and chromium targets, positioned symmetrically relative to the substrate holder, were used as cathode materials. The substrates were AISI 321 stainless steel (12X18H9T UA standard), previously mechanically polished to a mirror finish and ultrasonically cleaned in organic solvents. The selection of substrates was dictated by the requirements of optimal lattice matching, adequate thermal expansion compatibility with the AlN and CrN layers, and ensuring strong interfacial adhesion. Prior to coating deposition, the substrate surface was ion-cleaned in argon plasma at an elevated substrate bias to remove surface contaminants and activate the substrate.

Deposition parameters for all coatings are listed in Table 1. All MLCs were synthesized in a reactive nitrogen atmosphere at a constant pressure of 0.53 Pa. The nitrogen pressure was established through extensive preliminary experiments to identify the boundaries of the metallic-to-poisoned transition zone in the aluminum and chromium targets. At a nitrogen pressure of 0.53 Pa, nitrogen was insufficient to form nitride phases, and metallic dominated the coating composition. The selected value thus encompasses the complete transition from the formation of Al2N or Cr2N sub-nitrides to stable stoichiometric AlN and CrN. The negative substrate bias was varied to –50, –100, and –200 V, allowing investigation of the effect of ion bombardment energy on the structural evolution and composition of the coatings. The arc currents for the Cr and Al cathodes were maintained in the ranges of 105–110 A and 95–100 A, respectively, while the foil currents were adjusted within 0.4–0.5 A for Cr and kept at 0 A for Al. Minor variations in the arc and foil currents were introduced to stabilize the plasma discharge and compensate for target erosion, thereby ensuring a constant deposition rate and uniform plasma density across all processes. The deposition time for the AlN layers was systematically varied at 10, 40, and 60 seconds, while the CrN layer deposition parameters remained fixed. This variation was introduced to investigate the effects of evolution on phase, crystalline structure, elemental composition, and morphology.

Table 1. Technological parameters of AlN/CrN MLCs deposited by CA-PVD

AlN/CrN MLCs	Arc current (Cr/Al), A	Foil current (Cr/Al), A	Substrate bias, V	Nitrogen pressure, Pa	Deposition time Cr layer, s	Deposition time Al layer, s	Total deposition time, h	Bilayer quantity
1558	110/95	0.5/0	–50	0.53	10	10	1.65	70
1565	105/100	0.4/0	–100	0.53	10	40	1	72
1556	110/95	0.5/0	–200	0.53	10	60	1	55

Figure 1 shows a schematic of the CA-PVD deposition process for AlN/CrN MLCs. A chromium adhesion layer with a nanometer-scale thickness was first deposited to improve coating adhesion to the steel substrate. The multilayer structure was formed by periodically rotating the substrates relative to the evaporation sources, which ensured the sequential deposition of AlN and CrN layers. Three series of AlN/CrN MLCs were deposited with a bilayer number of 70, 72, and 55. The variation of a bilayer number was deliberately made to optimize the balance in total thickness of all MLCs and evaluate the same structural characteristics (including morphology, phase state and chemical composition).

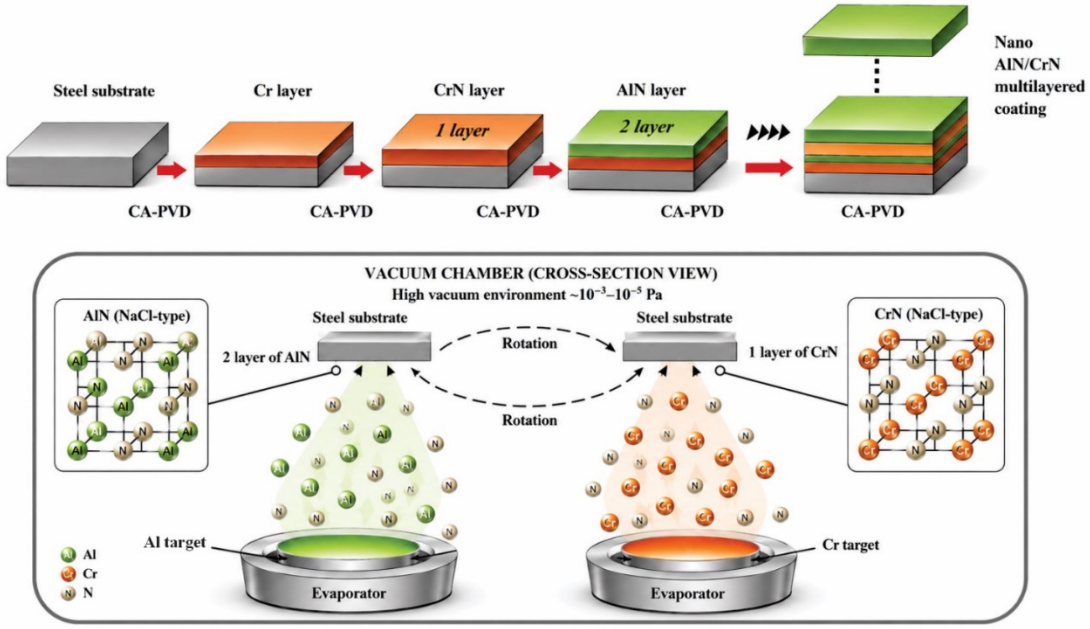

Figure 1. Schematic of AlN/CrN multilayer coating deposition by CA-PVD using separate Al and Cr targets with substrate rotation

2.2. Characterization

The surface morphology and topographic features of AlN/CrN MLCs were investigated by scanning electron microscopy (SEM) using a VEGA3 TESCAN scanning electron microscope. The microscopic analysis was conducted in the secondary electron (SE) detection mode to maximize surface-sensitive topographic contrast. The accelerating voltage of the primary electron beam (SEM HV) was maintained at 30.0 kV. The images were captured at working distances (WD) ranging between 15.07 mm and 19.72 mm. To ensure a comprehensive evaluation of the coating surface features, the analysis was performed across different scales: a low-magnification mode with a view field of 500 µm (utilizing a 100 µm scale bar) was used for overall surface overview. A high-magnification mode with a view field of 17.7 µm (utilizing a 10 µm scale bar) was employed for detailed examinations of localized surface fragments.

The phase composition and structural parameters of AlN/CrN MLCs were characterized by X-ray diffraction (XRD) analysis using a diffractometer operated in the “theta–2theta” geometry. The diffraction patterns were recorded utilizing Cu-Kα radiation (λ = 1.540600 A) generated from a Cu target at an operating voltage of 30.0 kV and a tube current of 30.0 mA. The optical system of the diffractometer was configured with a 1.0° divergence slit, a 1.0° scatter slit, and a 0.150 mm receiving slit. Data collection was performed in a continuous scanning mode over a 2theta angular range of 10.0°–100.0° at a scanning speed of 2.0°/min, a sampling pitch (step size) of 0.02°, and a preset time of 0.60 s per step. Phase identification, qualitative search-match analysis, and profile fitting were carried out using the Match! software package (Crystal Impact) linked with the International Center for Diffraction Data (ICDD) PDF-2 (Release 2004) reference database. The evaluation of the average crystallite size (sub-grain domain size) was performed via the Scherrer equation using a shape factor (Scherrer constant) of 0.94.

The elemental composition and distribution within the AlN/CrN MLCs were analyzed by energy-dispersive X-ray spectroscopy (EDS). The measurements were performed using an EDS detector integrated into the VEGA3 TESCAN scanning electron microscope. X-ray generation and spectrum collection were carried out over an energy range from 0 to 15 keV, recording characteristic emission intensities in counts per electron volt (cps/eV). Identification and deconvolution

of the overlapping elemental lines, specifically the low-energy light element region comprising Carbon (C-K), Nitrogen (N-K), and Aluminum (Al-K), alongside the transition metal series of Chromium (Cr-K), and Iron (Fe-K)), were executed using the integrated microscope software.

3. EXPERIMENTAL RESULTS

3.1. Surface structure

Figure 2 (left side) illustrates the surface morphology of AlN/CrN MLC deposited at a substrate bias of –50 V. The low-magnification image (at a 100 μm scale) reveals a highly developed surface topography typical for arc-plated films, heavily populated by macroparticles (droplets). This droplet phase generation is directly linked to the liquid metal emission from the cathode spots at arc currents of 110 A (Cr) and 95 A (Al). A detailed analysis indicates a polydisperse distribution of the macroparticles. Large, irregularly shaped solidified splats with sizes ranging from 15 to 35 μm are randomly distributed across the surface, with a spatial frequency of approximately 40–80 μm between them. Spherical droplets of medium (2–8 μm) and submicron (less <1 μm) sizes are also observed. The high-magnification SEM image (at a 10 μm scale) shows that the large droplets underwent significant flattening upon high-velocity impact with the substrate before solidification.

Planimetric evaluation demonstrates that the droplet-free matrix occupies approximately 75–80% of the total surface area, while the macroparticles and associated boundary defects cover the remaining 20–25%. The substrate bias of –50 V provided insufficient ion bombardment energy to suppress or re-sputter these large metallic aggregates during growth. The surface matrix exhibits a fine-grained, slightly dome-like texture, which is possibly indicative of a dense, competitive columnar growth of the alternating AlN and CrN nanolayers (at 10 s deposition cycles).

The surface morphology of AlN/CrN MLC deposited at an increased negative substrate bias of –100 V and an asymmetric layer deposition time (Cr/Al = 10/40 s) is presented in Figure 2 (center side). The low-magnification SEM image (at a 100 μm scale) reveals a modified topography compared to the previous sample, characterized by a reduction in the count of sharp volumetric macroparticles and the appearance of distinct crater-like tracks and flattened rims. The high-magnification view (at a 10 μm scale) captures a large, complex-shaped solidified metallic splat (~20–25 μm in size) with highly flattened, smoothed boundaries. This morphological evolution is directly attributed to the higher substrate bias of –100 V, which enhances the kinetic energy of the incident ion flux. The intense ion bombardment induces a noticeable re-sputtering effect on the protruding elements of the liquid droplet phase and stimulates lateral adatom diffusion during crystallization.

Statistical image processing indicates that the defect-free matrix area expanded to approximately 82–85% of the total surface, leaving only 15–18% occupied by macroparticles and associated boundary defects. The extended deposition time of the AlN layer (40 s) acts as a planarizing factor, effectively encapsulating the underlying droplet-induced roughness. Under these energetic conditions, the surface matrix may have acquired a significantly denser, highly smoothed sub-microcrystalline surface texture with suppressed competitive columnar dome formation, thereby ensuring a more uniform multilayer architecture.

The surface morphology of AlN/CrN MLC, deposited at an elevated negative substrate bias of –200 V and an asymmetric growth cycle (Cr/Al = 10/60 s), is illustrated in Figure 2 (right side). The low-magnification SEM micrograph (at a 100 μm scale) reveals a significantly modified, flattened surface topography. The application of high-energy ion bombardment (–200 V) activates intense sub-surface atomic displacement and energetic re-sputtering processes, which fundamentally alter the macroparticle evolution. The high-magnification view (at a 10 μm scale) focuses on a highly deformed macrodefect boundary, highlighting the joint effect of intense ion shearing and matrix overgrowth. Under a strict ion-assisted regime at –200 V, the arriving high-velocity nitrogen and metal ions severely erode and flatten the protruding liquid metallic droplets ejected from the cathodes. The extended 60 s deposition window for the AlN layer allows the matrix to structurally assimilate and fragment the droplet inclusions, completely erasing sharp phase boundaries. The remaining defect fraction is represented by highly planarized splats and shallow, smoothed craters.

Planimetric image analysis reveals a noticeable reduction in the defect-free matrix area, which drops to approximately 65–70% of the total surface, while the macroparticle occupation and associated micro-craters expand to 30–35%. This topographical degradation indicates that at an extreme negative substrate bias of –200 V combined with an extended AlN deposition time of 60 s, a defect accumulation mechanism becomes dominant. The high-energy incident ion flux induces preferential re-sputtering of the growing nitride matrix, thereby exposing and topographically highlighting the heavier metallic droplets that possess lower sputtering yields.

A comparative analysis of the surface morphology across the three investigated AlN/CrN MLCs reveals a non-monotonic transition in growth mechanisms governed by the synergy of substrate bias and AlN deposition time. At a low substrate bias of –50 V and short symmetric cycles (Cr/Al = 10/10 s), the coating surface is characterized by sharp, open macroparticles covering up to 25% of the area within a typical competitive columnar matrix. Increasing the bias to –100 V with an asymmetric cycle (Cr/Al = 10/40 s) introduces an optimal energetic window where ion-induced re-sputtering flattens droplet boundaries and activates adatom mobility, successfully expanding the clean matrix fraction to its maximum of 82–85%. However, escalating the negative bias to an extreme value of –200 V coupled with a prolonged 60 s AlN cycle triggers a severe over-bombardment regime. In this state, the clean matrix area shrinks back to 65–70% due to preferential ion etching of the nitride phases, which accentuates and exposes the un-sputtered metallic droplet aggregates. This severe ion-assisted treatment effectively suppresses the standard competitive columnar growth but yields

a highly stressed, fragmented, and topographically developed nanostructured surface architecture with the highest defect density among the altered parameters.

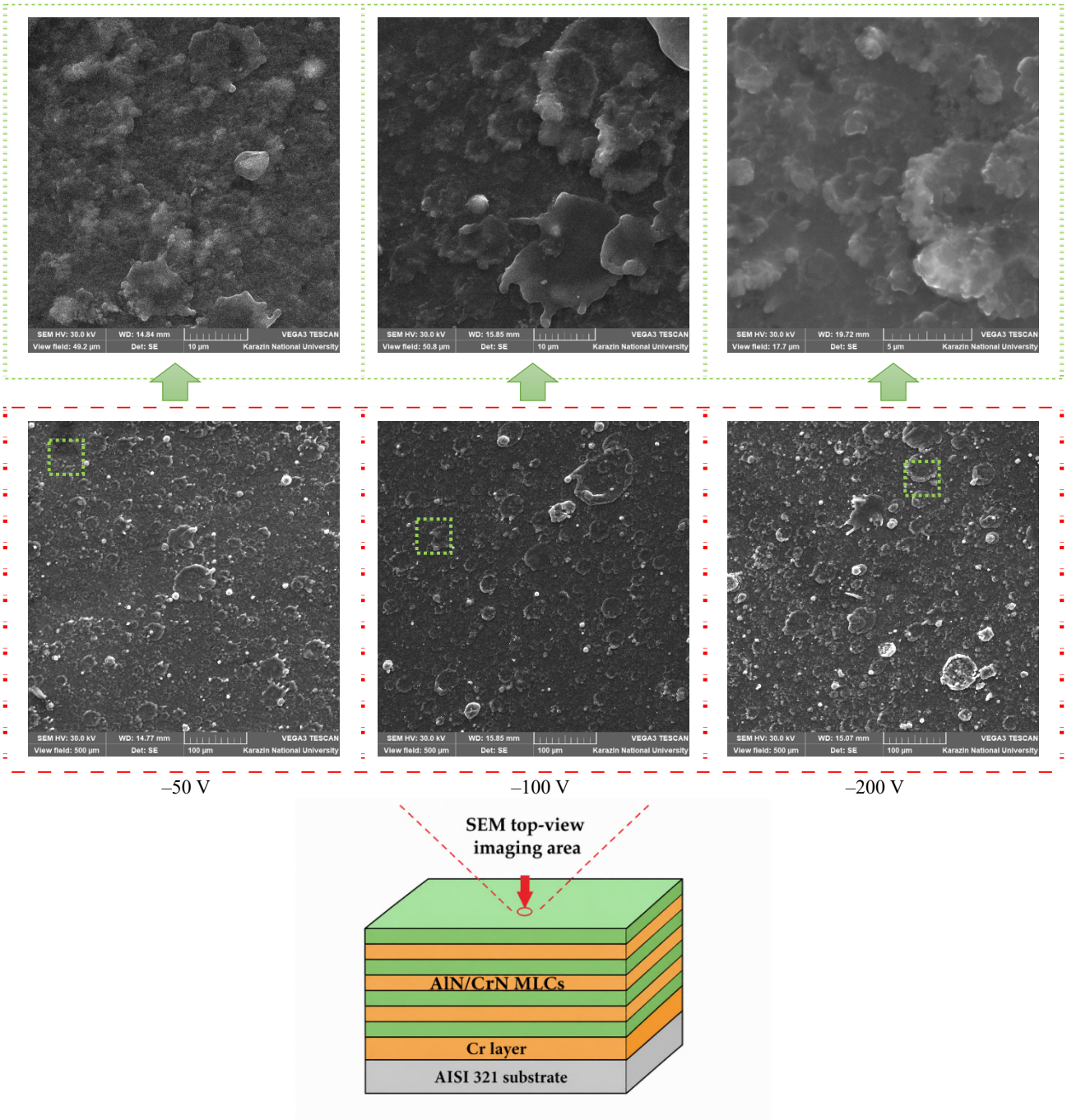

Figure 2. SEM images of AlN/CrN multilayer coatings deposited by CA-PVD at different substrate biases –50 V (left side), –100 V (center side) and –200 V (right side)

3.2. Structural-phase state

X-ray structural analysis of AlN/CrN MLCs, presented in Figure 3, reveals a heterophase crystalline structure. This structure consists of a mixture of stable cubic chromium nitride (c-CrN) with a NaCl-type structure, metastable cubic aluminum nitride (c-AlN) also possessing a NaCl-type structure, and stable hexagonal aluminum nitride (h-AlN) with a wurtzite structure.

On the X-ray pattern of AlN/CrN MLC deposited at substrate bias of –50 V, a doublet of peaks in the interval 2theta ≈ 32–36° is clearly visible. The first broad maximum at 2theta = 35.51° is formed due to the superposition of the h-AlN(002) and c-CrN(111) planes. The presence of the c-AlN(111) conjugate peak at 2theta = 38.43° confirms that with an ultrashort deposition time (10 s) the c-CrN lattice exerts a strong stabilizing (epitaxial) effect, forcing a significant part of the AlN phase to crystallize in the metastable cubic modification. A weak reflex of the hexagonal h-AlN(100) phase is

also recorded at 2theta ≈ 32.6°. The presence of a pronounced peak at 2theta = 64.87° (c-AlN(220) / h-AlN(103)) probably indicates that the coating has a polycrystalline structure with developed interphase boundaries.

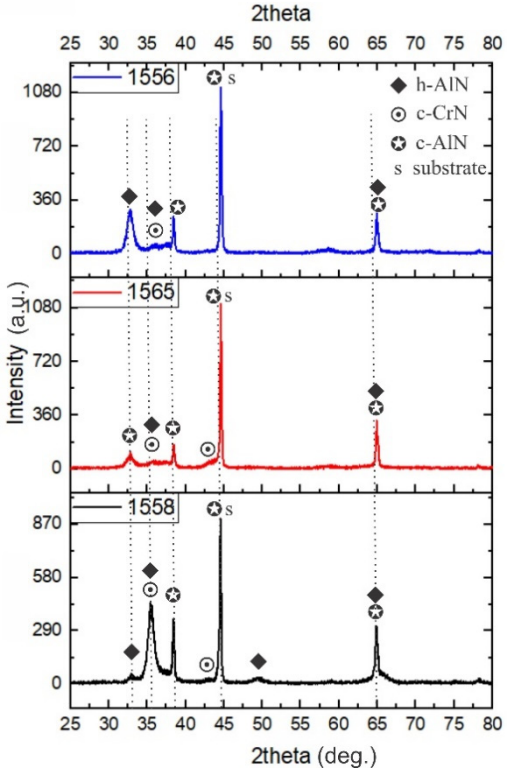

Figure 3. XRD patterns of AlN/CrN multilayer coatings deposited by CA-PVD at different substrate biases: –50 V (bottom pattern), –100 V (center pattern) and –200 V (top pattern)

For the following AlN/CrN MLC, increasing the deposition time of the AlN layer to 40 s, in combination with increasing the substrate bias to –100 V, radically changes the thermodynamics and kinetics of the transformed phases. A sharp drop in intensity and a significant broadening of all diffraction maxima of the coating in the range 2θ ≈ 32-40° are observed. The peak at 2θ = 36.07° (h-AlN/c-CrN) practically levels off, transforming into a diffuse halo. The observed changes are caused by two factors. First, the growth of the bias potential to –100 V intensifies ion bombardment, destructuring the crystal lattice and grinding the grain to a nanocrystalline or quasi-amorphous state. Secondly, increasing the thickness of the AlN layer (40 s) removes the system from the zone of epitaxial influence of cubic c-CrN. Within the AlN layer, a competition between the metastable cubic and stable hexagonal phases leads to strong internal microstresses, an increase in the density of packing defects, and a decrease in the intensity of the XRD signal.

For AlN/CrN MLC, an extreme increase in substrate bias to –200 V and a long growth cycle of AlN (60 s) shifts the structural mechanism towards radiation-stimulated phase segregation. A pronounced "return" of peak intensity is observed. The X-ray pattern is dominated by a clear, intense, and relatively narrow peak at 2theta = 32.75°, corresponding to the h-AlN(100) plane. At the same time, the peak at 2theta = 37.48° becomes low-intense and broad, and the reflex of cubic c-AlN(111) at 2theta = 38.47° again acquires an increase of intensity. The long continuous operation time of the aluminum evaporator (60 s) under hard ion assistance (–200 V) provides excess kinetic and thermal energy to the adatoms. This initiates the processes of dynamic return (recrystallization) and grain coalescence. The AlN phase is completely freed from epitaxial clamping on the part of c-CrN (since the layer becomes too thick) and thermodynamically relaxes into its stable hexagonal wurtzite form with a pronounced preferential orientation (texture) along the (100) plane.

Table 2. Summarized X-ray parameters of AlN/CrN MLCs deposited by CA-PVD at different substrate biases

2 theta, deg.	d-spacing, A	Identified phase	Crystallographic plane (*hkl*)	PDF card No.
32.75-32.89	2.7211-2.7319	h-AlN	(100)	01-070-2543
35.51-37.48	2.5260-2.7312	h-AlN/c-CrN	(002)/(111)	01-070-2543/00-011-0065
38.43-38.47	2.3404-2.3383	c-AlN	(111)	00-046-1200
43.75	2.0676	c-CrN	(200)	00-011-0065
44.56-44.61	2.0295-2.0315	substrate+c-AlN	(200)	00-046-1200
49.37	1.8444	h-AlN	(102)	01-070-2543
64.87-64.93	1.4349-1.4361	substrate+(h-AlN+c-AlN)	(220)+(103)	01-070-2543/00-046-1200

The average crystallite size for all investigated AlN/CrN MLCs was evaluated via the Scherrer formula, using the diffraction data of the most intense (dominant) textured peak corresponding to the hexagonal h-AlN modification. It was

established that variations in the deposition parameters exert a significant influence on the orientational stability and structural dispersion of the coatings. Specifically, for the AlN/CrN MLC obtained at substrate bias of –50 V and equal layer deposition times (Cr/Al = 10/10 s), the dominant reflection appears at 2theta = 35.51°, which is characterized by the minimum crystallite size in the series, measuring 13±2 nm. With an increase in the negative bias to –100 V and a prolonged aluminum layer growth duration (Cr/Al = 10/40 s), a shift in the preferred orientation is observed. The peak at 2theta = 32.81° becomes dominant, while the grain size slightly increases to 16±2 nm. This indicates an intensification of the hexagonal phase crystallization process under conditions of increased AlN layer thickness. A further increase in the energy of the bombarding ions at a bias of –200 V and an asymmetric deposition time (Cr/Al = 10/60 s) localizes the main diffraction maximum at 2theta = 32.75°. Concurrently, a minor reduction in the grain size down to 14±2 nm was recorded. This dynamic is attributed to enhanced ion re-sputtering and the generation of high residual stresses under extreme substrate biases, which ultimately restricts the diffusion growth of the crystallites.

3.3. Elemental composition

The elemental composition analysis of AlN/CrN MLCs deposited at various negative substrate biases (–50 V, -100 V, and –200 V) is presented in Table 3 and Figure 3.

Table 3. Elemental composition of AlN/CrN MLCs deposited by CA-PVD at different substrate biases: –50 V, –100 V, and –200 V

AlN/CrN MLCs	Substrate bias, V	Cr/Al deposition time, s	Elemental composition, at.%					
			Al	Cr	N	C	Fe	Total
1558	–50	10/10	46.88	6.15	45.94	0.68	0.35	100
1565	–100	10/40	45.21	18.37	35.69	0.26	0.47	100
1556	–200	10/60	33.72	21.21	44.31	0.14	0.62	100

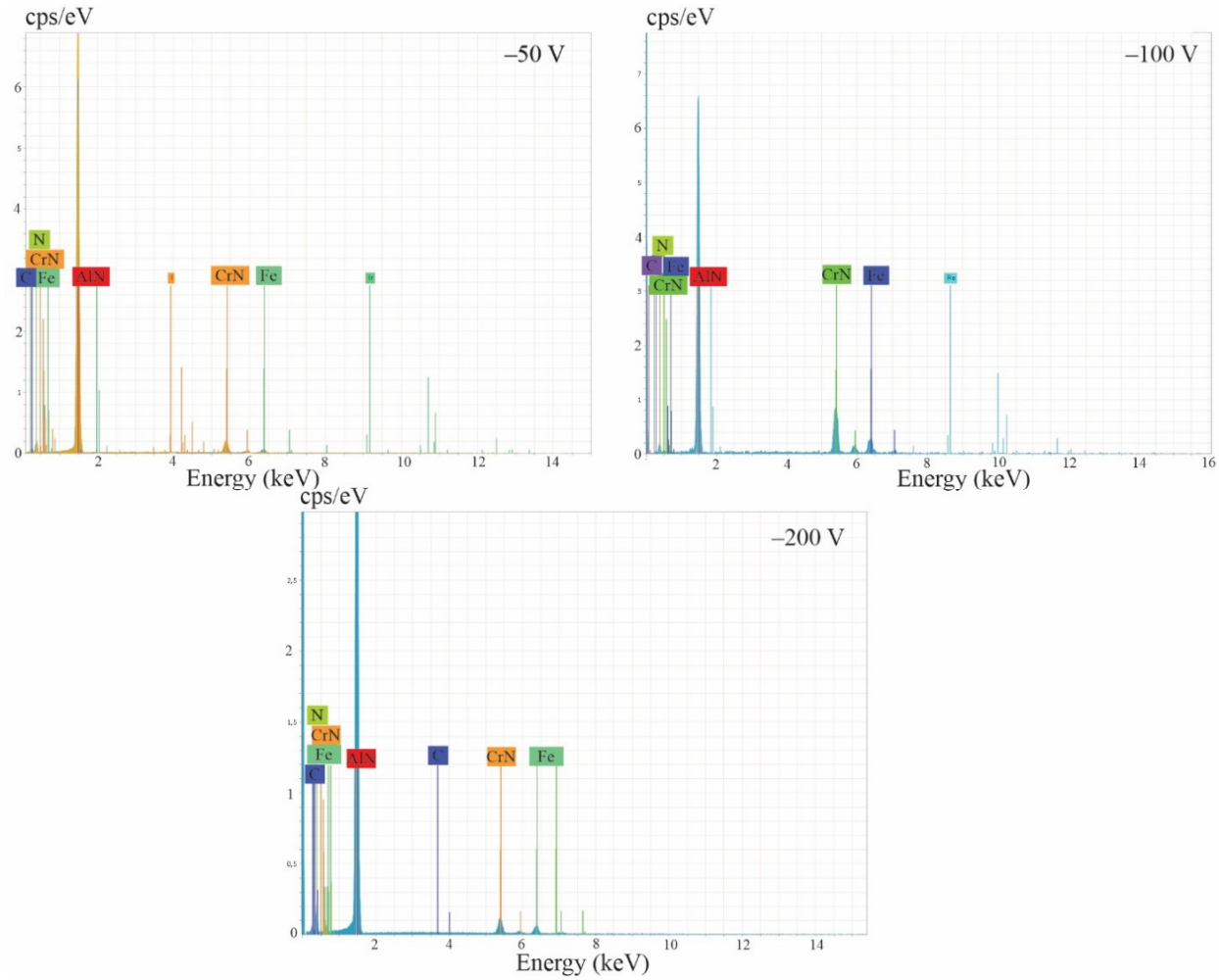

Figure 3. EDS spectra of AlN/CrN multilayer coatings deposited by CA-PVD at different substrate biases: –50 V (left spectrum), –100 V (right spectrum) and –200 V (center spectrum)

The elemental composition of the AlN/CrN MLC deposited at a substrate bias of –50 V and equal layer growth times (Cr/Al = 10/10 s) exhibits a high aluminum concentration of 46.88 at. %. The chromium content is minimal, at 6.15 at. %,

resulting in a high Al/Cr atomic ratio. Nitrogen constitutes 45.94 at. %, which is close to the stoichiometric ratio expected for a dominant AlN phase mixed with a smaller fraction of CrN. Trace amounts of carbon (0.68 at. %) and iron (0.35 at. %) are also detected within the coating matrix.

As the negative substrate bias is increased to –100 V and the aluminum layer deposition time is prolonged to 40 s (Cr/Al = 10/40 s), the elemental composition undergoes a noticeable transition. Despite the fourfold increase in the Al layer deposition time, the aluminum content slightly decreases to 45.21 at.%. Concurrently, the chromium concentration increases significantly to 18.37 at. %, while the nitrogen content drops to 35.69 at. %, suggesting a variation in phase stoichiometry. The carbon impurity level drops to 0.26 at. %, whereas the iron concentration slightly increases to 0.47 at. %.

At the highest negative substrate bias of –200 V and maximum aluminum layer deposition duration (Cr/Al = 10/60 s), a counterintuitive elemental distribution is observed. The aluminum content drops significantly to 33.72 at. %, representing the lowest Al concentration in the series. In contrast, the chromium content reaches a maximum of 21.21 at. %, while the nitrogen content returns to 44.31 at.%. The concentration of carbon impurities is minimized to 0.14 at. %, while the iron content reaches its peak value of 0.62 at. %.

In summary, elemental composition analysis of the investigated AlN/CrN MLCs revealed a counterintuitive decrease in the aluminum concentration (from 46.88 to 33.72 at. %) along with a concomitant increase in the chromium content as the ion bombardment energy was elevated. This phenomenon is driven by the preferential re-sputtering of the lighter aluminum atoms (m_{Al} = 26.98 amu vs. m_{Cr} = 52.00 amu) under the influence of high-energy ions at a substrate bias of -200 V, which effectively counteracts the effect of the prolonged Al layer deposition time. The presence of iron (0.35-0.62 at. %) is attributed to ion-stimulated interdiffusion from the AISI 321 stainless steel substrate, whereas the reduction in carbon content (down to 0.14 at.%) at higher negative biases is explained by the ion cleaning effect, which promotes the desorption of impurities.

High bias energies at –200 V induce severe lattice distortion, vacancy generation, and stress-driven diffusion. Under these extreme conditions, the thermodynamically more stable CrN phase suppresses the growth of metastable Al-containing phases. Consequently, the excess aluminum may be displaced to the grain boundaries, forming amorphous interlayers, or undergoes continuous secondary re-sputtering by plasma ions, thereby reducing its overall atomic fraction as detected by energy-dispersive X-ray spectroscopy (EDS).

4. DISCUSSIONS

4.1. Correlation between Deposition Parameters, Composition, and Phase Evolution

The structural and compositional evolution of the synthesized AlN/CrN MLCs is governed by a complex interplay of thermodynamics and kinetics. This behavior is dictated by the simultaneous modification of the negative substrate bias voltage (–50 V to –200 V) and the systematic expansion of the AlN layer growth window (t_{Al} = 10, 40, 60 s).

The epitaxial template effect is dominant at low deposition energies (–50 V, 10 s). At this stage, the incoming adatoms possess relatively low kinetic energy. The crystallization process is dominated by the structural constraint of the underlying cubic CrN template (B1, NaCl-type) [12]. Due to the minimal thickness of the AlN layer, the interface strain energetically minimizes the volume free energy required for the formation of the metastable cubic AlN modification (c-AlN), space group (Fm3m) [13]. This template effect forces a significant portion of AlN to mirror the rock-salt structure of CrN, as confirmed by the strong c-AlN(111) reflection at 2theta = 38.43°. At this stage, the hexagonal wurtzite phase h-AlN is possibly suppressed, manifesting with an isolated h-AlN(100) peak.

The competitive phase boundary disruption appears during mid-deposition energies (–100 V, 40 s). Transitioning to substrate bias of –100 V while simultaneously lengthening the AlN deposition step to 40 s breaks this pseudomorphic growth state. The increased layer thickness shifts the upper boundary of the AlN layer far beyond the spatial envelope of the epitaxial clamping exerted by the c-CrN lattice. As a result, the AlN phase attempts to relax into its thermodynamically stable hexagonal configuration (h-AlN, B4 wurtzite type). The overlap of competing tetrahedral (hexagonal) and octahedral (cubic) coordination matrices produces a localized structural mismatch [14]. This structural conflict manifests on the XRD profiles as severe peak attenuation and the formation of a diffuse halo in the 2theta ≈ 32–40° interval. Concurrently, the elevated ion bombardment at –100 V induces widespread lattice defects and grain refinement, reducing the long-range crystalline order to a quasi-amorphous state [15].

The radiation-stimulated segregation and coalescence start to dominate at high-deposition energies (–200 V, 60 s). At these parameters, the structural mechanism shifts entirely toward radiation-stimulated phase segregation and thermal relaxation [15]. High-velocity ion flux (N^+) delivers extensive kinetic energy directly to the film surface. This energy accelerates localized atomic displacement and adatom mobility. Because the 60 s growth interval yields an Al-rich environment independent of the CrN template, the excess energy facilitates dynamic recrystallization and grain coalescence. The AlN system completely escapes the interfacial strain of CrN, allowing the phase to crystallize into its highly textured, stable hexagonal wurtzite form along the h-AlN(100) plane at 2theta = 32.75°.

4.2. Analytical Insight into Mass-Dependent Preferential Re-sputtering Mechanisms

The elemental tracking shown in Table 3 reveals an unexpected composition profile: the net atomic concentration of Al drops from 46.88 at.% to 33.72 at.% despite a sixfold increase in the Al-target evaporation time. This compositional shift is driven by the physics of ion-surface interactions under varying acceleration potentials.

This phenomenon is governed by the discrepancy in atomic mass between the constituent transition metal and the principal group-III element (m_{Al} = 26.98 amu versus m_{Cr} = 52.00 am) [16]. According to classical cascade sputtering theories, the energy transfer coefficient (γ) during a binary atomic collision is maximized when the masses of the incident projectile particle (m_1, e.g., N^+) and the target atom (m_2) are closely matched:

$$\gamma = \frac{4m_1m_2}{(m_1 + m_2)^2}$$

Because the mass of nitrogen (m_N = 14.01 amu) sits closer to that of aluminum than chromium, energy transfer to the Al sublattice is highly efficient. At a low bias of –50 V, the incident ion energy remains below the threshold required for meaningful sub-surface sputtering, preserving the nominal deposition rates and yielding an Al/Cr ratio. When the potential is increased to –200 V, the kinetic energy of the incoming ions spikes, intensifying selective (preferential) re-sputtering of the lighter Al atoms from the growing layer. Conversely, the heavier Cr atoms exhibit a lower sputtering yield under these conditions and remain securely bound within the matrix. This process shifts the overall film stoichiometry toward a lower Al atomic fraction and compresses the Al/Cr ratio [17]. The high-energy ion bombardment at –200 V also generates high residual compressive stresses and a high concentration of point defects (vacancies and interstitials). Under these conditions, the thermodynamically stable CrN phase exhibits a lower free energy of formation and a higher cohesive energy compared to the metastable cubic AlN phase. This difference suppresses the retention of metastable c-AlN. The structural stress forces the excess, unbonded aluminum out of the primary lattice. This displaced aluminum either migrates via stress-driven diffusion to the grain boundaries – forming thin, amorphous AlN_x interlayers – or is stripped from the surface by continuous secondary plasma ion erosion.

4.3. Analysis of Impurities (C and Fe)

The inclusion of trace impurities provides additional insight into the CA-PVD deposition environment.

The carbon (0.68 to 0.14 at.%) acts as a typical residual interstitial impurity, originating from background hydrocarbons in the vacuum chamber (10^{-3}–10^{-5} Pa). At –50 V, these volatile carbon species easily co-condense onto the cold adatom sites. Raising the bias voltage to –20 V activates an ion cleaning effect [18]. The energetic ion flux imparts sufficient momentum to break weak C-C and C-metal bonds, desorbing these weakly adhered contaminants and driving the carbon content down to a negligible 0.14 at.%.

The iron (0.35 to 0.62 at.%) trace shows an opposite trend, increasing alongside the negative substrate bias. Since the coatings are deposited on an AISI 321 stainless steel substrate, this iron signature is driven by ion-stimulated interdiffusion at the film-substrate interface. The high-energy ion bombardment at –50 V creates forward-recoil atom displacements and a high density of point defects within the near-surface layers of the steel substrate [19]. This defect network acts as a series of high-speed diffusion pathways, prompting Fe atoms to migrate upward into the initial chromium adhesion layer and the subsequent AlN/CrN nanostructure.

CONCLUSIONS

This paper establishes the regularities governing the formation of the atomic-crystalline architecture, surface topography, and chemical composition of CA-PVD AlN/CrN multilayer coatings. Based on a comprehensive analysis (XRD, SEM/EDS), the following conclusions were drawn.

1. Three distinct structural regimes of phase evolution were identified. At low deposition energies (–50 V, 10 s), the epitaxial template effect of the c-CrN matrix dominates, stabilizing the metastable cubic c-AlN phase. A bias of –100 V (40 s) breaks down the pseudomorphic growth, transitioning the system into a nanocrystalline state. At an extreme bias potential of –200 V (60 s), complete thermal relaxation occurs, accompanied by a textured phase transition into stable hexagonal wurtzite h-AlN(100).
2. The evolution of surface topography is governed by the deposition energy. The –100 V regime was identified as optimal, where the intensified ion flux smooths the macroparticle boundaries, expanding the defect-free matrix to 82–85%. At –200 V, an over-bombardment regime takes over, triggering selective etching of the nitride phase and exposing heavier metallic droplets.
3. The elemental composition changes were determined. A counterintuitive decrease in Al concentration (from 46.88 to 33.72 at. %) was recorded despite the prolonged growth time. This phenomenon is driven by the mass-dependent selective re-sputtering of lighter Al atoms under high-energy ion flux. Increasing the bias voltage activates an ion-cleaning effect that reduces carbon contamination (down to 0.14 at. %), but simultaneously stimulates iron interdiffusion from the steel substrate into the coating (increasing up to 0.62 at. %).

The insights obtained expand the current understanding of non-equilibrium solid-state thermodynamics and open new avenues for the precision engineering of nanostructured protective coatings.

Acknowledgments

This work was supported by the Ministry of Education and Science of Ukraine (MES) under the National Budget Program (Project 0124U001127).

ORCID

Olga Maksakova, https://orcid.org/0000-0002-0646-6704; **Vyacheslav Beresnev**, https://orcid.org/0000-0002-4623-3243;
Serhii Lytovchenko, https://orcid.org/0000-0002-3292-5468; **Ruslan Galushkov**, https://orcid.org/0000-0002-9105-9774

REFERENCES

[1] W. Cheng, J. Wang, X. Ma, P. Liu, P.K. Liaw, and W. Li, "A Review on Microstructures and Mechanical Properties of Protective Nano-Multilayered Films," J. Mater. Res. Technol. **27**, 2413–2442 (2023). https://doi.org/10.1016/j.jmrt.2023.10.012

[2] B. Warcholinski, A. Gilewicz, P. Myslinski, E. Dobruchowska, and D. Murzynski, "Structure and Properties of AlCrN Coatings Deposited Using Cathodic Arc Evaporation," Coatings, **10**(8), 793 (2020). https://doi.org/10.3390/coatings10080793

[3] A.E. Reiter, V.H. Derflinger, B. Hanselmann, T. Bachmann, and B. Sartory, "Investigation of the properties of $Al_{1-x}Cr_xN$ coatings prepared by cathodic arc evaporation," Surf. Coat. Technol. **200**, 2114–2122 (2005). https://doi.org/10.1016/j.surfcoat.2005.01.043

[4] K. Lukaszkowicz, J. Sondor, A. Paradecka, M. Pawlyta, B. Chmiela, M. Pancielejko, B. Szczucka-Lasota, *et al*., "Structure and Tribological Properties of AlCrN + CrCN Coating," Coatings, **10**(11), 1084 (2020). https://doi.org/10.3390/coatings10111084

[5] J.F. Tang, C.Y. Lin, F.C. Yang, and C.L. Chang, "Influence of nitrogen content and bias voltage on residual stress and the tribological and mechanical properties of CrAlN films," Coatings, **10**(6), 546 (2020). https://doi.org/10.3390/coatings10060546

[6] H. Cao, J. Yang, Y. Li, L. Ren, F. Qi, N. Zhao, Y. Zhou, *et al*., "Effect of nitrogen pressure on the microstructure, mechanical and electrochemical properties of CrAlN coatings deposited by filter cathode vacuum arc," Ceramics International, **48**(24), 36570-36584 (2022). https://doi.org/10.1016/j.ceramint.2022.08.216

[7] C. Sabitzer, J. Paulitsch, S. Kolozsvári, R. Rachbauer, and P.H. Mayrhofer, "Impact of bias potential and layer arrangement on thermal stability of arc evaporated Al-Cr-N coatings," Thin Solid Films, **610**, 26–34 (2016). https://doi.org/10.1016/j.tsf.2016.05.011

[8] A.D. Pogrebnyak, A.P. Shpak, N.A. Azarenkov, and V.M. Beresnev, "Structures and properties of hard and superhard nanocomposite coatings," Physics-Uspekhi, **52**(1), 29 (2009). https://doi.org/10.3367/UFNe.0179.200901b.0035

[9] S. Liu, Y. Yang, R. Ji, X.T. Zeng, and W.J. Clegg, "AlN/CrN multilayer structures with increased thermal stability," Scripta Materialia, **130**, 242-246 (2017). https://doi.org/10.1016/j.scriptamat.2016.12.020

[10] W-C. Huang, and H-W. Chu, "Influence of Layer Configuration on the Morphology and Corrosion Resistance of CrAlN/TiSiN Multilayer Coatings Prepared via Cathodic Arc Deposition," Coatings, **16**(6), 658 (2026). https://doi.org/10.3390/coatings16060658

[11] J. Nyman, M. Junaid, N. Sarius, J. Birch, S. Kahl, and H. Högberg, "Substrate bias effects on cathodic arc deposited Cr coatings," Results in Materials, **19**, 100450 (2023). https://doi.org/10.1016/j.rinma.2023.100450

[12] Z. Chen, D. Holec, M. Bartosik, P.H. Mayrhofer, and Z. Zhang, "Crystallographic orientation dependent maximum layer thickness of cubic AlN in CrN/AlN multilayers," Acta Materialia, **168**, 190-202 (2019). https://doi.org/10.1016/j.actamat.2019.02.004

[13] M. Bartosik, M. Todt, D. Holec, J. Todt, L. Zhou, H. Riedl, H. J. Böhm, *et al*.,."Thermal expansion of rock-salt cubic AlN," Applied Physics Letters, **107**(7), 071602 (2015). https://doi.org/10.1063/1.4928911

[14] B. Alling, A.V. Ruban, A. Karimi, O.E. Peil, S.I. Simak, L. Hultman, and I.A. Abrikosov, "Mixing and decomposition thermodynamics of *c*−Ti1−*x*Al*x*N from first-principles calculations," Physical Review B, **75**(18), 045123 (2007). https://doi.org/10.1103/PhysRevB.75.045123

[15] J. Musil, "Hard and superhard nanocomposite coatings," Surface and Coatings Technology, **125**(1-3), 322-330 (2000). https://doi.org/10.1016/S0257-8972(99)00586-1

[16] G. Greczynski, J. Lu, M. Johansson, J. Jensen, I. Petrov, J.E. Greene, and L. Hultman, "Selection of metal ion irradiation for controlling Ti1-xAlxN alloy growth via hybrid HIPIMS/magnetron co-sputtering," Vacuum, **86**(8), 1036-1040 (2012). https://doi.org/10.1016/j.vacuum.2011.10.027

[17] Z. Zhang, and M.G. Lagally, "Atomistic Processes in the Early Stages of Thin-Film Growth," Science, **276**(5311), 377-383 (1997). https://doi.org/10.1126/science.276.5311.37

[18] A. Metel, Y. Bublikov, Y. Melnik, C. Sotova, F. Milovich, A. Seleznev, *et al*., "Features of the Process of Surface Preparation of Products Using Glow Discharge Plasma During the Deposition of Modifying Coatings," Journal of Composites Science, **9**(12), 640 (2025). https://doi.org/10.3390/jcs9120640

[19] X. Li, B. Bakhit, M.P. Johansson Jõesaar, L. Hultman, I. Petrov, and G. Greczynski, "Toward energy-efficient physical vapor deposition: Routes for replacing substrate heating during magnetron sputter deposition by employing metal ion irradiation," Surface and Coatings Technology, **415**, 127120 (2021). https://doi.org/10.1016/j.surfcoat.2021.127120

ЕПІТАКСІАЛЬНА СТАБІЛІЗАЦІЯ ТА РАДІАЦІЙНО-СТИМУЛЬОВАНА СЕГРЕГАЦІЯ У БАГАТОШАРОВИХ ПОКРИТТЯХ AlN/CrN, ОТРИМАНИХ МЕТОДОМ CA-PVD ЗА УМОВ ІОННОГО БОМБАРДУВАННЯ

О.В. Максакова, В.М. Береснєв, С.В. Литовченко, Р.С. Галушков

Харківський національний університет імені В.Н. Каразіна, майдан Свободи, 4, 61000 Харків, Україна

У цій роботі досліджено закономірності формування атомно-кристалічної архітектури, топографії поверхні та хімічного складу багатошарових покриттів AlN/CrN, осаджених методом катодно-дугового фізичного осадження з парової фази на підкладки з аустенітної нержавіючої сталі AISI 321. Проаналізовано синергетичний вплив від'ємної напруги зміщення до підкладки (від –50 до –200 В) та тривалості осадження індивідуальних шарів AlN (10, 40 і 60 с) на кінетику фазової конкуренції та еволюцію радіаційно-стимульованих наноструктур. Методами рентгенівської дифракції та растрової електронної мікроскопії у поєднанні з енергодисперсійною рентгенівською спектроскопією встановлено, що за низьких енергій осадження (–50 В, 10 с) домінує ефект епітаксіального шаблону матриці c-CrN, тим самим стабілізуючи метастабільну кубічну фазу c-AlN. Збільшення як товщини шару, так і напруги зміщення до –100 В призводить до руйнування псевдоморфного росту та

переводить систему в ймовірний нанокристалічний або квазіаморфний стан. За високого потенціалу зміщення –200 В відбувається повна термічна релаксація, що супроводжується текстурованим фазовим переходом AlN у його стабільну гексагональну модифікацію вюрциту (h-AlN). Спостерігалося контр-інтуїтивне зниження концентрації алюмінію (з 46,88 до 33,72 ат.%), незважаючи на тривалий час росту . Цей феномен зумовлений селективним перерозпиленням легших атомів Al під дією високоенергетичного іонного потоку. Крім того, було зафіксовано радіаційно-стимульовану інтердифузію заліза з підкладки у покриття, разом із ефектом іонного очищення, який видаляє домішки впровадження вуглецю з матриці. Отримані результати розширюють поточне розуміння нерівноважної термодинаміки твердого тіла та відкривають нові можливості для прецизійного проєктування властивостей наноструктурних захисних покриттів шляхом оптимізації іонно-плазмових параметрів.

Ключові слова: *вакуумно-дугова технологія; нітриди; багатошарові покриття; AlN; CrN; мікроструктура; хімічний склад; фазовий стан*